

# ShapeMoiré: Channel-Wise Shape-Guided Network for Image Demoiréing

Jinming Cao, Sicheng Shen, Qiu Zhou, Yifang Yin, Yangyan Li, and Roger Zimmermann *Senior Member, IEEE*

**Abstract**—Photographing optoelectronic displays often introduces unwanted moiré patterns due to analog signal interference between the pixel grids of the display and the camera sensor arrays. This work identifies two problems that are largely ignored by existing image demoiréing approaches: 1) moiré patterns vary across different channels (RGB); 2) repetitive patterns are constantly observed. However, employing conventional convolutional (CNN) layers cannot address these problems. Instead, this paper presents the use of our recently proposed *Shape* concept. It was originally employed to model consistent features from fragmented regions, particularly when identical or similar objects coexist in an RGB-D image. Interestingly, we find that the *Shape* information effectively captures the moiré patterns in artifact images. Motivated by this discovery, we propose a ShapeMoiré method to aid in image demoiréing. Beyond modeling shape features at the patch-level, we further extend this to the global image-level and design a novel Shape-Architecture. Consequently, our proposed method, equipped with both ShapeConv and Shape-Architecture, can be seamlessly integrated into existing approaches without introducing additional parameters or computation overhead during inference. We conduct extensive experiments on four widely used datasets, and the results demonstrate that our ShapeMoiré achieves state-of-the-art performance, particularly in terms of the PSNR metric. We then apply our method across four popular architectures to showcase its generalization capabilities. Moreover, our ShapeMoiré is robust and viable under real-world demoiréing scenarios involving smartphone photographs. We open-sourced an implementation of ShapeMoiré in PyTorch at <https://github.com/ShapeMoiré>.

**Index Terms**—Moiré Pattern, Image Demoiréing, Image Restoration, Shape Information

## I. INTRODUCTION

Moiré artifacts appear as wavy or rippled distortions in digital photographs. This unwanted pattern is caused by the interference between the color filter array of cameras and the

This research is supported by the National Research Foundation, Singapore, and Ministry of National Development, Singapore, under its Cities of Tomorrow R&D Programme (CoT Award NRF-CoT-V4-2020-9). Any opinions, findings and conclusions or recommendations expressed in this material are those of the author(s) and do not reflect the views of National Research Foundation, Singapore (NRF), Ministry of National Development, Singapore (MND), National Parks Board, Singapore (NParks), and Housing Development Board, Singapore (HDB). We would also like to acknowledge NParks for the comments and assistance with providing locality information and images of flora and fauna used in this project.

Jinming Cao, Sicheng Shen and Roger Zimmermann are with National University of Singapore, Singapore. E-mail: jinming.ccao@gmail.com, sshen@u.nus.edu, rogerz@comp.nus.edu.sg.

Qiu Zhou is with Beijing university of posts and telecommunications, China. E-mail: zhouqiulv@gmail.com.

Yifang Yin is with Institute for Infocomm Research (I<sup>2</sup>R), A\*STAR, Singapore. E-mail: yin\_yifang@i2r.a-star.edu.sg.

Yangyan Li is with Alibaba Group, China. E-mail: yangyan.lee@gmail.com.

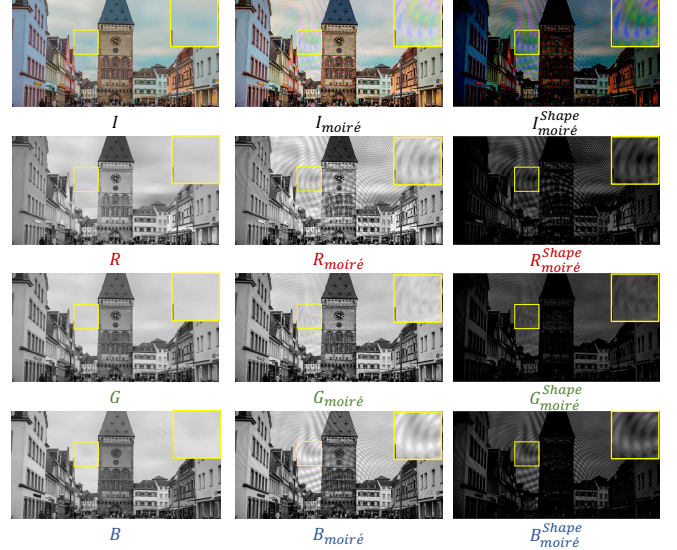


Fig. 1. Visual demonstration of the moiré pattern in the given image and its separate manifestations in the individual RGB channels. Left column: the original image  $I$ , where the color in each channel is uniformly and smoothly distributed; Middle column: it can be observed that the three channels of  $I_{\text{moiré}}$  display distinct moiré patterns; Right column: the shapes of moiré patterns in the *shape* space ( $R_{\text{Shape moiré}}$ ,  $G_{\text{Shape moiré}}$  and  $B_{\text{Shape moiré}}$ ) remain consistent with the patterns in the different channels of the original moiré image ( $R_{\text{moiré}}$ ,  $G_{\text{moiré}}$  and  $B_{\text{moiré}}$ ), but with enhanced structural integrity.

sub-pixel arrangement of displays. Fig. 1 illustrates a digital photo with such moiré patterns ( $I_{\text{moiré}}$ ), which make the original image ( $I$ ) appear opaque and distorted when displayed on a screen. Notably, the irregular shape and wide frequency span of moiré patterns distinguish demoiréing from other image restoration tasks such as super-resolution [1], [2] and reducing JPEG compression artifacts [3].

Moiré pattern removal has attracted extensive research interests over the past few years [4]–[8]. Initially, efforts were devoted to collecting synthetic data [9] or genuine images with low resolution [10]. Subsequent datasets expanded the image resolution to 1080P [6] or even ultra-high-definition (4K) [7], posing greater challenges in removing moirés without compromising the pristine features of the images. To address this, prior methods have mostly relied on rich side information, such as complementary visual attributes [5] and aliasing frequencies [11], [12]. Despite the advancements in existing methods, they often treat the input image from a holistic perspective, especially without discriminating between different channels (i.e., RGB channels). However, as observed in Fig. 1, unlike the uniform and smooth color distribution

in each channel ( $R$ ,  $G$  and  $B$ ) of the original image  $I$ , these three input channels ( $R_{\text{moiré}}$ ,  $G_{\text{moiré}}$  and  $B_{\text{moiré}}$ ) typically exhibit distinct moiré patterns. As a result, processing them equally with convolutional layers confuses the model’s focus on demoiréing, resulting in sub-optimal outcomes. Furthermore, existing literature often overlooks the repetitive patterns that are consistently observed.

Our idea in this work is inspired by a recent prevailing concept—*Shape*—in RGB-D segmentation [13]. Unlike traditional CNNs, ShapeConv [13] can distinguish between different channels and is adept at modeling repetitive shapes, such as two identical chairs in a depth image from RGB-D segmentation. In the context of moiré patterns in an image, as demonstrated in Fig. 1, the moiré image ( $I_{\text{moiré}}$ ) exhibits frequent similar or repetitive patterns, unlike the uniform color distribution in the original image ( $I$ ). This type of information is precisely what *shape* excels at expressing. Additionally, the features of moiré patterns in the *shape* space ( $R_{\text{moiré}}^{\text{Shape}}$ ,  $G_{\text{moiré}}^{\text{Shape}}$  and  $B_{\text{moiré}}^{\text{Shape}}$ ) remain consistent across different channels of the original moiré image ( $R_{\text{moiré}}$ ,  $G_{\text{moiré}}$  and  $B_{\text{moiré}}$ ), but with enhanced structural integrity. This result motivates us to approach the image demoiré problem from the *shape* perspective.

Therefore, we propose a novel method named ShapeMoiré to extend our ShapeConv for image demoiréing. Our ShapeMoiré operates on both patch<sup>1</sup>-level and image-level shapes. This results in two key components of our proposed ShapeMoiré: the Shape-aware convolutional layer (ShapeConv) and Shape-aware network architecture (Shape-Architecture). Specifically, at the patch-level, we first decompose a patch into two separate components, i.e., a *base-component* and a *shape-component*. We then employ two operations, namely, base-product and shape-product, to process these components respectively with two learnable weights: the base-kernel and the shape-kernel. The output from these operations are then combined in an addition manner to form a shape-aware patch, which is subsequently convolved with a standard convolutional kernel. Unlike the original patch, the shape-aware patch is capable of adaptively learning the shape characteristic with the shape-kernel, while the base-kernel serves to balance the contributions of the *shape* and the *base* components in the final feature representation. For the extended image-level, we incorporate an additional training stream to enhance the model’s focus on shape information during training. This is achieved by adding a loss function for the shape branch, thereby updating the parameters with an emphasis on shape information. In a nutshell, the former replaces the conventional convolutional layer with a delicately designed ShapeConv that involves the modeling of shape features, and the latter employs the shape information of raw pixels to further enhance the baseline architecture. It is worth noting that our ShapeMoiré can be seamlessly integrated into most baseline architectures that are equipped with convolutional layers as building blocks. In addition, benefiting from its original virtue, our ShapeMoiré results in no incremental parameters and very negligible com-

putational cost.

To evaluate the effectiveness of our proposed method, we conducted extensive experiments on four well-established datasets: LCDMoiré [9], TIP2018 [10], FHDMi [6], and UHDM [7]. Our experimental results demonstrate that ShapeMoiré outperforms existing state-of-the-arts by a significant performance margin. To assess its generalization capabilities, we applied ShapeMoiré to various widely adopted demoiréing architectures [7], [10], [11] and observed improved results compared to baselines. Notably, qualitative results highlight that ShapeMoiré remarkably enhances moiré pattern removal, even when applied to real-world images captured using a smartphone. This underscores both the effectiveness on public datasets and the practical applicability of our ShapeMoiré in real-world scenarios.

The work on ShapeConv has previously been published at ICCV [13]. This extended manuscript expands upon the original version in several key aspects:

- We broaden the application of the notion of *Shape* beyond its original use in RGB-D segmentation. For the first time, this concept has been effectively applied to the task of removing moiré pattern in 2D images.
- Beyond employing patch-level ShapeConv, we introduce an image-level Shape-Architecture for image demoiréing. Through ablation studies, we have demonstrated that the *Shape* information at different levels can enhance performance on this challenging task.
- The proposed ShapeMoiré method, which incorporates both ShapeConv and Shape-Architecture, represents a versatile approach. We conduct experiments using various existing methods as baselines, all of which effectively enhance baseline performance. Notably, both ShapeConv and Shape-Architecture introduce ZERO additional parameters and negligible computational overhead during inference.

## II. RELATED WORK

### A. Image Demoiréing

Removing moiré patterns constitutes a form of image denoising aimed at mitigating the destructive artifacts arising from frequency interference during image capture. Unlike other types of noise, such as flickering [14] induced by photography, there is currently no standard tool for effectively eliminating moiré patterns. Recently, numerous benchmark datasets and approaches have been introduced to address the challenge of image demoiréing.

a) *Datasets*: Liu et al. [15] initiated the task by curating a synthetic dataset that simulates the process of photographing with a camera. Building upon this approach, Yuan et al. [9] developed a large-scale synthetic dataset, namely, LCDMoiré, for further image demoiréing [9], [12], [16]. However, the transition from synthetic training to real-world scenarios presents a significant obstacle due to the inherent gap between simulation and reality. Sun et al. [10] addressed this challenge by introducing the TIP2018 dataset, which utilizes real-world moiré images. Following this approach, Yue et al. [8] compiled a well-aligned dataset of raw moiré image. Nevertheless, these

<sup>1</sup>The operational unit of input features for the convolutional layer, whose spatial size matches that of the convolution kernel.



images often have low resolutions, making it difficult for the accompanying methods to adapt to high-resolution images. To tackle this issue, He et al. [6] curated the FHDMi dataset with a resolution of 1080P. However, as the demand for image quality continues to increase, the practicality of 1080p resolution may diminish, especially when considering the ultra-high-definition (4K) images captured by modern mobile cameras. Recognizing these challenges and limitations, Yu et al. [7] collected the first ultra-high-definition demoiré dataset (UHDM), which contains 5,000 real-world 4K resolution image.

*b) Methods:* Pertaining to moiré pattern removal methods, current approaches often endeavor to design specific architectures for this task. For example, He et al. [5] proposed to classify moiré patterns using manually annotated category labels. Some more approaches [11], [12] have focused on the frequency domain via de-aliasing. In order to remove moiré without compromising the clarity of underlying image details, Sun et al. [10] implemented a multi-scale network, DMCNN, effectively addressing moiré patterns in practical scenarios. Building upon DMCNN, He et al. [6] developed the multi-stage framework FHDe<sup>2</sup>Net to handle a wider pattern scale range and preserve fine details. For 4K images, ESDNet [7] implements an efficient module that is semantic-aligned and scale-aware to address the scale variation of moiré patterns.

Unlike previous methods, which treat the entire image as a whole without distinguishing between different channels, Yang et al. [4] also observed differences in moiré patterns across different RGB channels. Specifically, they found that the red (R) and blue (B) channels are more heavily affected by moiré artifacts compared to the green (G) channel. Therefore, they proposed to remove moiré artifacts in the R and B channels using guided filtering based on the texture layer obtained from the G channel. In contrast to the method in [4], our approach does not involve special treatment of a specific channel but instead presents a universal method that discriminates between different channels. Moreover, [4] is a specialized design, while our proposed ShapeMoiré stands out as a versatile approach. It can seamlessly integrate with existing methods, enhancing model performance with ZERO increase of memory and computation.

## B. Image Restoration

Image restoration aims to reconstruct the original, clean and high-quality image from degraded versions. This task encompasses various processes, including image super-resolution (SR), image denoising, reducing JPEG compression artifacts and so on. A plethora of learning-based image restoration models [17], [18], [18], [19], have gained popularity due to their impressive performance. These models typically leverage large-scale paired datasets to learn mappings between low-quality and high-quality images, employing encoder-decoder structures [20] or hierarchical architectures [10], [21]. Building upon pioneering works such as SRCNN [22] (for SR), DnCNN [23] (for denoising), and ARCNN [3] (for reducing JPEG artifacts), numerous CNN-based models [24]–[26] have emerged. These models enhance representational capacity by incorporating larger and deeper neural architectures, such as residual blocks [27], dense blocks [28], and others [24].

## C. Shape Concept and Its Applications

The concept of *Shape* was initially introduced in the domain of RGB-D segmentation in a previously published paper [13], where it is defined as the disparity between local depth values and the overall distance of the region from the observation point. One key observation from this paper is that, in spaces where identical or similar objects coexist, *Shape* can extract more consistent features compared to raw pixel values. To leverage this insight, we designed ShapeConv to replace traditional convolution layers, allowing for the processing of data from various modalities while emphasizing *Shape* attributes. Subsequent studies [29], [30] extended the application to remote sensing data, showcasing *Shape*'s superiority in feature extraction across RGB+nDSM (primarily representing height features) data modalities. Specifically, Xiong et al. [29] utilized ShapeConv for semantic segmentation tasks on the their collected GAMUS dataset, which features numerous repetitive buildings. Zhong et al. [30] created an ocean coral dataset characterized by repetitive texture patterns within the corals. By integrating ShapeConv as a fundamental component of their model, they achieved superior performance. Beyond the RGB+X data, [31] employs ShapeConv for 3D object detection and occupancy.

This paper represents the first application of the *Shape* notion to 2D tasks. In particular, we observe that the moiré patterns tend to be repetitive across channel, aligning with the features that *Shape* learns. Additionally, we propose an application of *Shape* at the global image-level, namely the Shape-Architecture, to complement the patch-level ShapeConv. Our experimental results demonstrate a distinct advantage of *Shape* when the input data changes from 3D to 2D. This showcases the versatility of the *Shape* concept and holds promise for broader applications.

## III. METHOD

In this section, we first provide the basic formulation of the Shape-aware convolutional layer (ShapeConv), followed by its application in the training and inference phase. Subsequently, we delve into the comprehensive framework of the Shape-aware network architecture (Shape-Architecture), elucidating its data flow dynamics during both training and inference stages. Finally, we present the ShapeMoiré method, equipped with ShapeConv and Shape-Architecture.

### A. ShapeConv

*a) Method Intuition:* Given an input image with a moiré pattern,  $I_{\text{moiré}}$ , image demoiré aims to remove these unwanted patterns and thereby restore the original pristine image. Existing methods [6], [7], [10], [11] often involve an encoder-decoder framework, wherein the conventional convolutional layer serves as the core building block. A convolutional layer takes as input a feature map, either raw pixels or intermediate image features, in a sliding window manner. It typically comprises multiple convolution kernels, which are applied to a patch of images at each window position. To facilitate our discussion, we conceptualize one image patch as a 3D tensor  $\mathbb{P} \in \mathbb{R}^{K_h \times K_w \times C_{in}}$ ,  $K_h$  and  $K_w$  are the spatial dimensions of

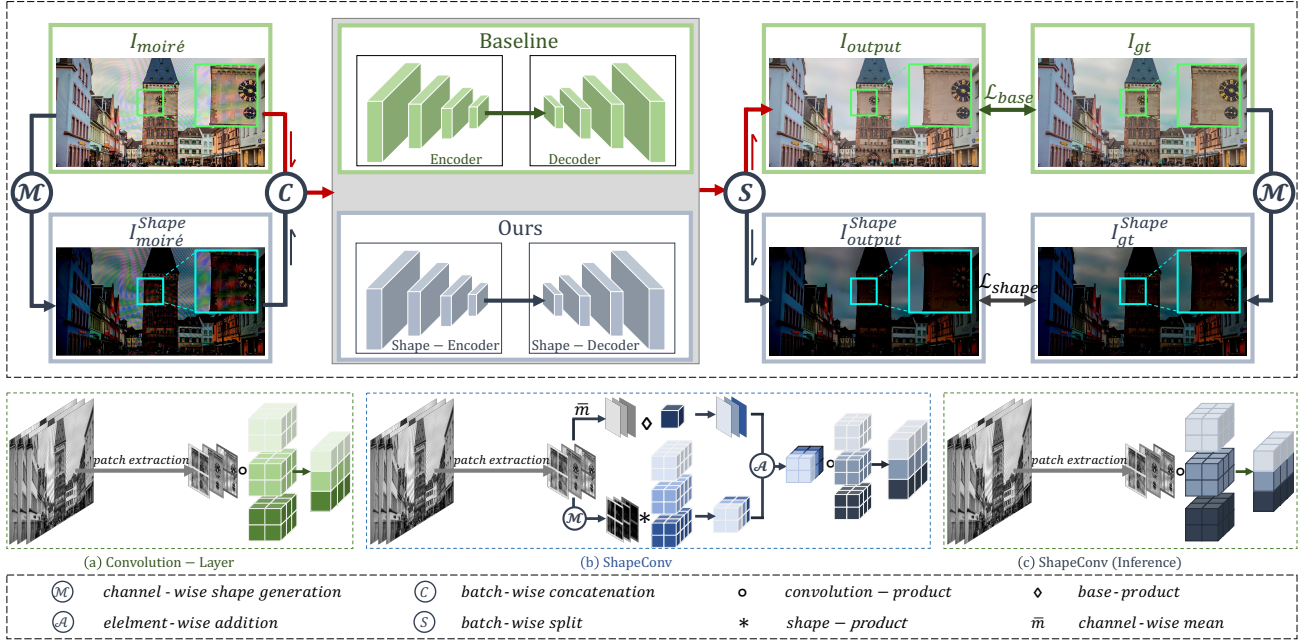


Fig. 2. Overview of ShapeMoiré. The top part depicts the network’s overall architecture. The green and blue parts denote the baseline and ShapeMoiré components, respectively, and the red line flow represents ShapeMoiré during inference. The bottom part shows network layers: (a) Convolution-Layer (consistent in both training and testing), and (b) and (c) illustrate ShapeConv during training and inference, respectively. For both ShapeConv and Shape-Architecture, our method introduces no parameters and negligible computational cost during inference.

the kernel and  $C_{in}$  represents the channel numbers in the input feature map. The output features from the vanilla convolution layer are obtained by,

$$\mathbb{F} = \text{Conv}(\mathbb{K}, \mathbb{P}), \quad (1)$$

where  $\mathbb{K} \in R^{K_h \times K_w \times C_{in} \times C_{out}}$  denotes the learnable weights of kernels in a convolutional layer (The bias terms are not included for simplicity.) and  $C_{out}$  represents the number of channels in the output feature map. Each element of  $\mathbb{F} \in R^{C_{out}}$  is calculated as,

$$\begin{cases} \mathbb{F} = \mathbb{K} \circ \mathbb{P} \\ \mathbb{F}_{C_{out}} = \sum_i^{K_h \times K_w \times C_{in}} (\mathbb{K}_{i, C_{out}} \times \mathbb{P}_i). \end{cases} \quad (2)$$

where the  $\circ$  denotes the convolution-product. We show one example in Fig. 2(a) (best view in color), where  $K_h = K_w = 2$ ,  $C_{in} = 3$  (featuring distinct input channels represented by various square frame colors), and  $C_{out} = 3$ .

**b) ShapeConv Formulation:** Based on the aforementioned analysis, in this paper, we offer to decompose an input patch into two components: a base-component  $\mathbb{P}_B$  and a shape-component  $\mathbb{P}_S$ . Specifically, we refer to the mean of patch values to be  $\mathbb{P}_B$ , and its relative values to be as  $\mathbb{P}_S$ :

$$\begin{aligned} \mathbb{P}_B &= \bar{m}(\mathbb{P}), \\ \mathbb{P}_S &= \mathcal{M}(\mathbb{P}) = \mathbb{P} - \bar{m}(\mathbb{P}), \end{aligned} \quad (3)$$

where  $\bar{m}(\mathbb{P})$  is the channel-wise mean function on  $\mathbb{P}$  (over the  $K_h \times K_w$  dimensions), with  $\mathbb{P}_B \in R^{1 \times 1 \times C_{in}}$ , and  $\mathbb{P}_S \in R^{K_h \times K_w \times C_{in}}$ .

Note that directly convolved  $\mathbb{P}_S$  with  $\mathbb{K}$  in Equation 1 is sub-optimal, as the values from  $\mathbb{P}_B$  contribute significantly to key discrimination across patches. Therefore, our ShapeConv

approach utilizes two learnable weights,  $\mathbb{W}_B \in R^1$  and  $\mathbb{W}_S \in R^{K_h \times K_w \times K_h \times K_w \times C_{in}}$ , to separately process these two components. The resulting features are then combined through element-wise addition, creating a new channel-wise shape-aware patch with the same size as the original  $\mathbb{P}$ . The formulation of ShapeConv is given as,

$$\begin{aligned} \mathbb{F} &= \text{ShapeConv}(\mathbb{K}, \mathbb{W}_B, \mathbb{W}_S, \mathbb{P}) \\ &= \text{Conv}(\mathbb{K}, \mathbb{W}_B \diamond \mathbb{P}_B + \mathbb{W}_S * \mathbb{P}_S) \\ &= \text{Conv}(\mathbb{K}, \mathbf{P}_B + \mathbf{P}_S) \\ &= \text{Conv}(\mathbb{K}, \mathbf{P}_{BS}), \end{aligned} \quad (4)$$

where  $\diamond$  and  $*$  denote the base-product and shape-product operator, respectively, which are defined as,

$$\begin{cases} \mathbf{P}_B = \mathbb{W}_B \diamond \mathbb{P}_B \\ \mathbf{P}_{B_{1,1,C_{in}}} = \mathbb{W}_B \times \mathbb{P}_{B_{1,1,C_{in}}}, \end{cases} \quad (5)$$

$$\begin{cases} \mathbf{P}_S = \mathbb{W}_S * \mathbb{P}_S \\ \mathbf{P}_{S_{k_h, k_w, C_{in}}} = \sum_i^{K_h \times K_w} (\mathbb{W}_{S_{i, k_h, k_w, C_{in}}} \times \mathbb{P}_{S_{i, C_{in}}}), \end{cases} \quad (6)$$

where  $C_{in}$ ,  $k_h$ ,  $k_w$  are the indices of the elements in  $C_{in}$ ,  $K_h$ ,  $K_w$  dimensions, respectively.

We reconstruct the channel-wise shape-aware patch  $\mathbf{P}_{BS}$  through the addition of  $\mathbf{P}_B$  and  $\mathbf{P}_S$ , where  $\mathbf{P}_{BS} \in R^{K_h \times K_w \times C_{in}}$ , enabling it to be smoothly convolved by the kernel  $\mathbb{K}$  of a vanilla convolutional layer. However,  $\mathbf{P}_{BS}$  is equipped with the important shape information which is learned by two additional weights. The operation of the ShapeConv is depicted at the bottom of Fig. 2(b).

### B. ShapeConv in Training and Inference

a) *Training phase*: The proposed ShapeConv can effectively leverage the *shape* information of patches. However, replacing the vanilla convolutional layer with ShapeConv in CNNs introduces more computational cost due to the two *product* operations in Equation 5 and 6. To tackle this problem, we propose shifting these two operations from patches to kernels,

$$\begin{cases} \mathbf{K}_B = \mathbb{W}_B \diamond \mathbb{K}_B \\ \mathbf{K}_{B_{1,1,C_{in},C_{out}}} = \mathbb{W}_B \times \mathbb{K}_{B_{1,1,C_{in},C_{out}}} \end{cases}$$

$$\begin{cases} \mathbf{K}_S = \mathbb{W}_S * \mathbb{K}_S \\ \mathbf{K}_{S_{k_h,k_w,C_{in},C_{out}}} = \sum_i^{K_h \times K_w} (\mathbb{W}_{S_{i,k_h,k_w,C_{in}}} \times \mathbb{K}_{S_{i,C_{in},C_{out}}}), \end{cases}$$

where  $\mathbb{K}_B \in R^{1 \times 1 \times C_{in} \times C_{out}}$  and  $\mathbb{K}_S \in R^{K_h \times K_w \times C_{in} \times C_{out}}$  denote the base-component of kernels and shape-component, respectively, and  $\mathbb{K} = \mathbb{K}_B + \mathbb{K}_S$ .

We therefore re-formalize ShapeConv in Equation 4 to:

$$\begin{aligned} \mathbb{F} &= \text{ShapeConv}(\mathbb{K}, \mathbb{W}_B, \mathbb{W}_S, \mathbb{P}) \\ &= \text{Conv}(\mathbb{W}_B \diamond \bar{m}(\mathbb{K}) + \mathbb{W}_S * \mathcal{M}(\mathbb{K}), \mathbb{P}) \\ &= \text{Conv}(\mathbb{W}_B \diamond \bar{m}(\mathbb{K}) + \mathbb{W}_S * (\mathbb{K} - \bar{m}(\mathbb{K})), \mathbb{P}) \\ &= \text{Conv}(\mathbb{W}_B \diamond \mathbf{K}_B + \mathbf{K}_S, \mathbb{P}) \\ &= \text{Conv}(\mathbf{K}_{BS}, \mathbb{P}), \end{aligned} \quad (7)$$

where  $\bar{m}(\mathbb{K})$  is the channel-wise mean function on  $\mathbb{K}$  (over the  $K_h \times K_w$  dimensions). And we require  $\mathbf{K}_{BS} = \mathbf{K}_B + \mathbf{K}_S$ ,  $\mathbf{K}_{BS} \in R^{K_h \times K_w \times C_{in} \times C_{out}}$ .

In fact, the two formulations of Shpe-Layer, i.e., Equation 4 and Equation 7 are mathematically equivalent, i.e.,

$$\begin{aligned} \mathbb{F} &= \text{ShapeConv}(\mathbb{K}, \mathbb{W}_B, \mathbb{W}_S, \mathbb{P}) \\ &= \text{Conv}(\mathbb{K}, \mathbf{P}_{BS}) \\ &= \text{Conv}(\mathbf{K}_{BS}, \mathbb{P}), \end{aligned} \quad (8)$$

$$\begin{aligned} \mathbb{F}_{C_{out}} &= \sum_i^{K_h \times K_w \times C_{in}} (\mathbb{K}_{i,C_{out}} \times \mathbf{P}_{BS_i}) \\ &= \sum_i^{K_h \times K_w \times C_{in}} (\mathbf{K}_{BS_{i,C_{out}}} \times \mathbb{P}_i), \end{aligned} \quad (9)$$

please refer to the Appendix for detailed proof. In this way, we utilize the ShapeConv in Equation 7 in our implementation as illustrated in Figure 3(b) and (c).

b) *Inference phase*: During inference, since the two additional weights i.e.  $\mathbb{W}_B$  and  $\mathbb{W}_S$ , become constants, we can fuse them into  $\mathbf{K}_{BS}$  as shown in Figure 3(c) with  $\mathbf{K}_{BS} = \mathbb{W}_B \diamond \mathbb{K}_B + \mathbb{W}_S * \mathbb{K}_S$ . And  $\mathbf{K}_{BS}$  shares the same tensor size with  $\mathbb{K}$  in Equation 1, thus, our ShapeConv is actually the same as the vanilla convolutional layer in Figure 3(a). In this way, this operation introduces negligible computational and memory costs compared to the original convolution layer (see Fig. 2(a) and (c) for a visual comparison).

### C. Shape-Architecture

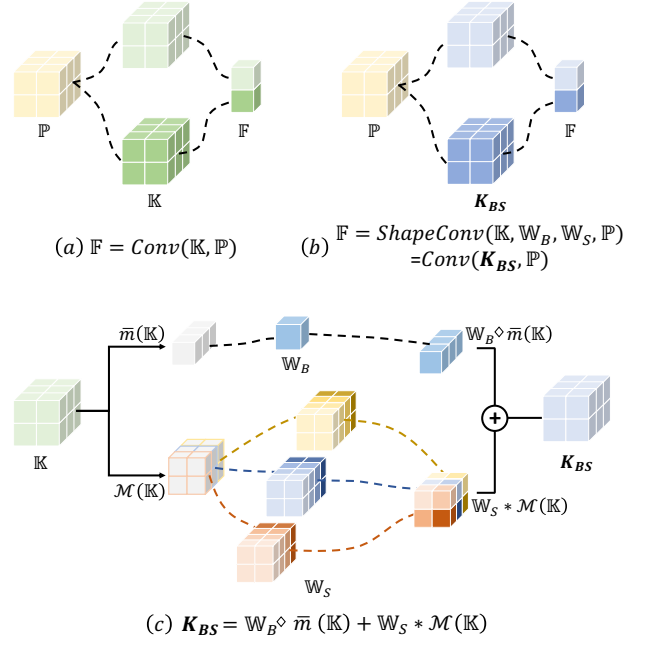


Fig. 3. Comparison of vanilla convolution layer and ShapeConv within a patch  $\mathbb{P}$ . In this figure,  $K_h = K_w = 2$ ,  $C_{in} = 3$ , and  $C_{out} = 2$ , “+” denotes element-wise addition. (a) Vanilla convolution with kernel  $\mathbb{K}$ ; (b) ShapeConv with folding the  $\mathbb{W}_B$  and  $\mathbb{W}_S$  into  $\mathbf{K}_{BS}$ ; (c) The computation of  $\mathbf{K}_{BS}$  from  $\mathbb{K}$ ,  $\mathbb{W}_B$  and  $\mathbb{W}_S$ .

a) *Method Intuition*: As depicted in Fig. 2 (top), the baseline network architecture (shown in green boxes) takes the image with moiré patterns, denoted as  $I_{moiré}$ , as input and produces the restoration image, denoted as  $I_{output}$ . Subsequently, the  $\mathcal{L}_{base}$  is computed by comparing  $I_{output}$  with the ground truth, represented as  $I_{gt}$ . The network parameters can then be updated using typical gradient descent algorithms. Current prevailing methods commonly utilize pixel-wise loss functions, such as  $L_1$  loss [34] and  $L_2$  loss [10], or a combination with the feature-based perceptual loss  $L_p$  [5], [7], [11]. In this context, we take the combination loss as an example,

$$\mathcal{L}_{base} = L_1(I_{output}, I_{gt}) + \lambda L_p(I_{output}, I_{gt}), \quad (10)$$

where  $\lambda$  is a hyperparameter that balances between  $L_1$  and  $L_p$ .

b) *Shape-Architecture*: The above ShapeConv primarily operates on intermediate features. To further explore the utility of *Shape* features, we leverage a Shape-Architecture to extract these features from the image-level. The Shape-Architecture complements the baseline network architecture with an additional *Shape* stream, as illustrated in the blue box and solid data flow in Fig. 2. To implement this, we first acquire the shape feature  $I_{moiré}^{Shape}$  from the input image. Thereafter, we input  $I_{moiré}^{Shape}$  to the same model and employ the ground-truth shape features,  $I_{gt}^{Shape}$  which are extracted from  $I_{gt}$ , for supervision,

$$\begin{aligned} I_{moiré}^{Shape} &= \mathcal{M}(I_{moiré}), \\ I_{gt}^{Shape} &= \mathcal{M}(I_{gt}), \end{aligned} \quad (11)$$



TABLE I  
PERFORMANCE COMPARISON WITH STATE-OF-THE-ART METHODS ON LCDMoiré, TIP2018, FHDMi, AND UHDM DATASETS. (↑) AND (↓) INDICATE BETTER PERFORMANCE WITH LARGER AND SMALLER NUMBERS, RESPECTIVELY. **RED**: BEST AND **BLUE**: SECOND-BEST.

Dataset	Metrics	Input	DMCNN (TIP18) [10]	MopNet (ICCV19) [5]	WDNet (ECCV20) [11]	MBCNN (CVPR20) [12]	ESDNet (ECCV22) [7]	SEDNet-L (ECCV22) [7]	DDA (ICLR23) [32]	RRID (arXiv24) [33]	ShapeMoiré
LCDMoiré [9]	PSNR↑	10.44	35.48	-	29.66	44.04	44.83	<b>45.34</b>	41.68	-	<b>46.56</b>
	SSIM↑	.5717	.9785	-	.9670	.9948	<b>.9963</b>	<b>.9966</b>	.9869	-	.9930
TIP2018 [10]	PSNR↑	20.3	26.77	27.75	28.08	30.03	29.81	<b>30.11</b>	-	-	<b>30.16</b>
	SSIM↑	.7380	.8710	.8950	.9040	.8930	<b>.9160</b>	<b>.9200</b>	-	-	.8795
FHDMi [6]	PSNR↑	17.97	21.54	22.76	-	22.31	24.5	<b>24.88</b>	23.62	24.39	<b>25.06</b>
	SSIM↑	.7033	.7727	.7958	-	.8095	.8351	<b>.8440</b>	.8293	.8300	<b>.8474</b>
	LPIPS↓	.2837	.2477	.1794	-	.1980	.1354	<b>.1301</b>	-	-	<b>.1306</b>
UHDM [7]	PSNR↑	17.12	19.91	19.49	20.36	21.41	22.12	<b>22.42</b>	-	-	<b>22.95</b>
	SSIM↑	.5089	.7575	.7572	.6497	.7932	.7956	<b>.7985</b>	-	-	<b>.8021</b>
	LPIPS↓	.5314	.3764	.3857	.4882	.3318	.2551	<b>.2454</b>	-	-	<b>.2415</b>

where  $\mathcal{M}$  aligns with the definition in ShapeConv, i.e., the subtraction from the channel-wise mean. Subsequently,  $I_{moiré}^{Shape}$  is batch-wisely concatenated with  $I_{moiré}$  and fed into the model, ensuring that these two streams remain uninterfered with each other. The model output is then split into  $I_{output}^{Shape}$  and  $I_{output}$ . Pertaining to the shape stream, the loss function  $\mathcal{L}_{shape}$  is obtained by,

$$\mathcal{L}_{shape} = L_1(I_{output}^{Shape}, I_{gt}^{Shape}) + \lambda L_p(I_{output}^{Shape}, I_{gt}^{Shape}). \quad (12)$$

The final loss function  $\mathcal{L}_{total}$  is:

$$\mathcal{L}_{total} = \mathcal{L}_{base} + \mathcal{L}_{shape}. \quad (13)$$

*c) Shape-Architecture During Inference:* Note that during training, the two streams share the same parameters. As a result, no parameters are introduced by our Shape-Architecture. We leverage  $\mathcal{L}_{shape}$  to make the parameters more aware of the shape features. Regarding the inference stage, in order to align with the structure of the baseline network architecture, we efficiently remove the shape stream from our Shape-Architecture, as illustrated in the red line flow in Fig. 2. Moreover, we employ this strategy to allow for seamless integration with baselines and avoid introducing any computational overheads.

#### D. ShapeMoiré

We term the approach equipped with both ShapeConv and Shape-Architecture as ShapeMoiré. This means our Shape-More operates on two hierarchical levels: 1) Patch-level: we replace all the convolutional layers with our ShapeConv; 2) Image-level: we complement the baseline network architecture with another shape-aware image stream. It is noteworthy that the two components, ShapeConv and Shape-Architecture, are independent of each other and can be separately added to baseline methods to enhance performance. As mentioned earlier, neither of these components introduces additional parameters or computational overhead during inference. Therefore, our approaches introduce ZERO parameters and incur negligible computation compared to the baseline method during inference. We will later demonstrate the complementary effect of these two components in our experiments.

## IV. EXPERIMENTS

**Datasets.** Our experiments were conducted using four publicly accessible datasets:

(1) LCDMoiré Dataset [9]. As a part of the AIM19 image demoiréing challenge, the LCDMoiré dataset comprises 10,200 synthetically generated image pairs. It is structured to include 10,000 images for training purposes, 100 images for validation, and another 100 for testing. Each image is of high resolution, with dimensions of  $1024 \times 1024$  pixels.

(2) TIP2018 Dataset [10]. This dataset consists of real photographs obtained by capturing images from ImageNet [35] displayed on computer screens, ensuring each image has a resolution of  $256 \times 256$  pixels.

(3) FHDMi Dataset [6]. It includes a substantial collection of 9,981 training image pairs and 2,019 testing pairs. All images in this dataset are in full high-definition resolution, measuring  $1920 \times 1080$  pixels.

(4) UHDM Dataset [7]. It stands out for its 4K resolution demoiréing capability. It is an ultra-high-resolution dataset featuring 5,000 image pairs that span a broad spectrum of scenes, including landscapes, sports, video clips, and documents. The dataset is notable for its diverse moiré patterns, produced using various device combinations and viewpoints. Each image in this dataset is  $3840 \times 2160$  pixels.

These datasets, ranging from synthetically generated pairs to ultra-high-resolution real photographs, offer a comprehensive platform for evaluating the effectiveness of our methods across different scenarios and image qualities.

**Evaluation Protocols.** For quantitative evaluation, we employed widely recognized metrics, including PSNR (Peak Signal-to-Noise Ratio), SSIM (Structure Similarity) [36], and LPIPS (Learned Perceptual Image Patch Similarity) [37]. In addition to these performance-related metrics, we also considered the network's parameter count, denoted as Param.(M), which indicates the number of network parameters in millions. This metric is pertinent to the overall memory usage of the network. It is important to note that previous methods [5], [7], [10], [11], [16] have exclusively reported PSNR and SSIM metrics on the TIP2018 and LCDMoiré datasets. In

TABLE II

PERFORMANCE COMPARISON WITH DIFFERENT BASELINE METHODS ON FOUR DATASETS. AN ASTERISK (\*) INDICATES THE PERFORMANCE WE REPRODUCED ON THE RESPECTIVE DATASETS USING THE SOURCE CODE PROVIDED BY DIFFERENT METHODS, NOTING SLIGHT DISCREPANCIES FROM THE ORIGINAL PUBLICATIONS.

Architecture	Method	UHDm [7]			FHDMi [6]			TIP2018 [10]		LCDMoiré [9]		Params. (M)
		PSNR↑	SSIM↑	LPIPS↓	PSNR↑	SSIM↑	LPIPS↓	PSNR↑	SSIM↑	PSNR↑	SSIM↑	
ESDNet [7]	Baseline*	22.253	.7974	.2511	24.393	.8392	.1366	29.791	.8753	45.286	.9921	5.934
	ShapeMoiré	22.597	.8007	.2490	24.629	.8402	.1336	29.862	.8758	45.537	.9925	5.934
	$\Delta$	0.344↑	.0033↑	.0021↓	0.236↑	.0010↑	.0030↓	0.071↑	.0005↑	0.251↑	.0004↑	0
ESDNet-L [7]	Baseline*	22.554	.7997	.2468	24.808	.8435	.1321	30.096	.8789	45.544	.9925	10.623
	ShapeMoiré	22.948	.8021	.2415	25.064	.8474	.1306	30.161	.8795	46.558	.993	10.623
	$\Delta$	0.394↑	.0024↑	.0053↓	0.256↑	.0039↑	.0015↓	0.065↑	.0006↑	1.014↑	.0005↑	0
WDNet [11]	Baseline*	19.181	.6417	.4271	21.161	.7714	.2411	27.812	.8381	37.324	.9721	3.36
	ShapeMoiré	19.882	.7442	.3272	22.182	.7901	.2134	28.312	.8535	38.408	.9782	3.36
	$\Delta$	0.701↑	.1025↑	.0999↓	1.021↑	.0187↑	.0277↓	0.500↑	.0154↑	1.084↑	.0061↑	0
DMCNN [10]	Baseline*	17.812	.7294	.5561	19.313	.7375	.3395	24.518	.8073	29.321	.9482	1.426
	ShapeMoiré	18.036	.7336	.5185	19.615	.7495	.2889	25.381	.8234	29.649	.9570	1.426
	$\Delta$	0.224↑	.0042↑	.0376↓	0.302↑	.0120↑	.0506↓	0.863↑	.0161↑	0.328↑	.0088↑	0

line with this convention, we adhere to the same setup for our comparisons.

**Implementation Details.** We adopted several popular approaches [7], [10], [11] as our baseline to demonstrate both the effectiveness and generalization capability of our proposed method. We strictly followed the original implementations of these baseline methods, except for the model components of ShapeMoiré. This guarantees that the observed performance improvements are solely attributable to the application of ShapeMoiré, yet not influenced by other factors. Unless otherwise noted, the baseline model is ESDNet-L [7]. Detailed implementations of our method can be found in our released code.

#### A. Comparison with State-of-the-Art Methods

We compared our method with state-of-the-art techniques and reported the results in Table I. As evident from the table, our ShapeMoiré significantly outperforms existing methods across most scenarios. It is noteworthy that our approach establishes a new SOTA across all four datasets in terms of the PSNR metric, which quantifies the level of noise or distortion compared to the original undistorted image. The results highlight that the modeled shape features in our ShapeMoiré play a crucial role in identifying the causal factors essential for image demoiréing. Furthermore, ShapeMoiré demonstrates superior performance compared to existing approaches on the UHDm dataset, emphasizing the effectiveness of our proposed method for Ultra-High-Definition images.

#### B. Generalization to Diverse Architectures

The proposed ShapeMoiré is a versatile approach that can be seamlessly integrated into existing methods for image demoiréing. To test its generalization capability, we applied our ShapeMoiré to four representative demoiréing methods, namely ECDNet [7], ECDNet-L [7], WDnet [11], and DM-CNN [10]. Table II demonstrates that ShapeMoiré consistently delivers significant performance improvements across ALL

settings. Moreover, our method introduces no additional inference cost compared to baselines, i.e., the added parameters are zero. It is worth noting that, as observed in Table II, the performance of current methods mostly correlates positively with the number of parameters. However, ShapeMoiré demonstrates the ability to enhance performance without increasing the network’s parameter count. For instance, our method achieves comparable (or even higher PSNR) performance to ESDNet-L (which has almost twice the parameter count of ESDNet) on the UHDm dataset, even when keeping the parameter count consistent with ESDNet.

#### C. Ablation Study

The two components we propose, ShapeConv and Shape-Architecture, are independent of each other. This means that adding either one of them to the baseline method alone can enhance the model’s performance. To validate the effectiveness of both components, we conducted detailed ablation studies. The results of these studies are presented in Table III. One can observe that the removal of both ShapeConv and Shape-Architecture leads to degraded model performance. Introducing either the ShapeConv or the Shape-Architecture yields a positive outcome. Combining these two together, i.e., our final ShapeMoiré, achieves the best results, highlighting their complementary effect on the overall model performance.

TABLE III  
ABLATION STUDY OF SHAPEMOIRÉ ON THE UHDm DATASET.

ShapeConv	Shape-Architecture	PSNR↑	SSIM↑	LPIPS↓
×	×	22.253	.7974	.2511
✓	×	22.469	.7990	<b>.2424</b>
×	✓	22.315	.7984	.2471
✓	✓	<b>22.597</b>	<b>.8007</b>	.2490

Additionally, we computed the inference time of both the baseline and our ShapeMoiré method. Specifically, we conducted this experiment on a single NVIDIA A40 GPU with 48G memory and ran both models for three runs. Subsequently, we calculated the average inference time for 5,000

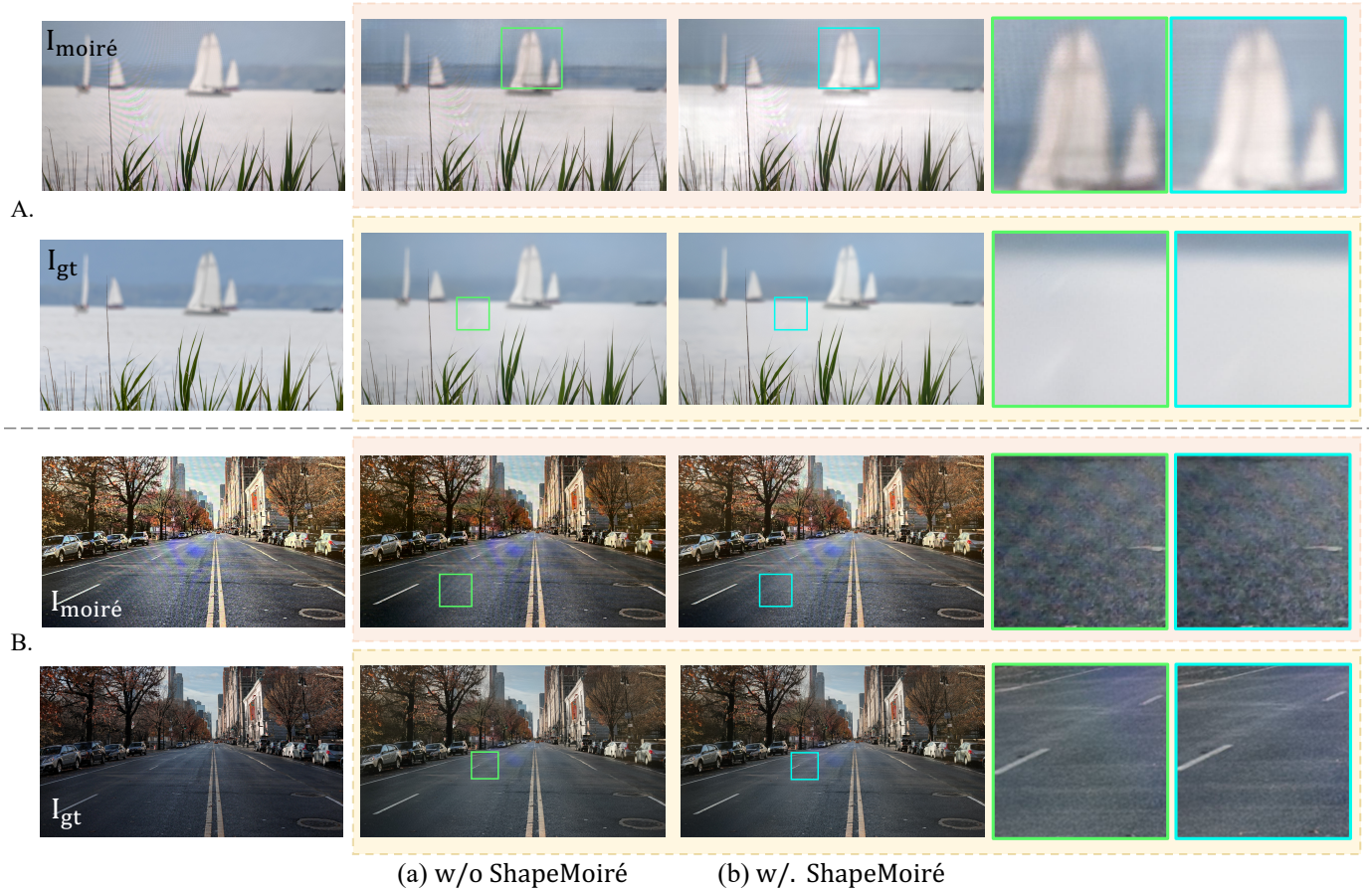


Fig. 4. Visualization results from the UHDM dataset. Larger boxes represent amplified views of the corresponding smaller colored border boxes, offering a clearer perspective when enlarged. For samples A and B, the top and bottom rows respectively depict the visualization results using WDNNet [11] and ESDNet-L [7] as baseline methods.

images and presented the milliseconds (ms) per image in Table IV. It is evident that our ShapeMoiré method imposes a very negligible overhead on the baseline model in most cases and even runs faster than the baseline due to clock time oscillation. This results validate the efficiency of the proposed ShapeMoiré method.

TABLE IV  
INFERENCE TIME COMPARISON OF BASELINE AND OUR SHAPEMOIRÉ ON THE UHDM DATASET.

Architecture	Method	ms/image		
		run1	run2	run3
ESDNet [7]	Baseline	7.70	8.00	7.80
	ShapeMoiré	8.30	8.04	7.98
WDNet [11]	Baseline	6.79	7.07	6.62
	ShapeMoiré	6.72	7.01	7.06
DMCNN [10]	Baseline	2.17	1.96	1.91
	ShapeMoiré	1.95	2.07	2.21

#### D. Visualization

In Fig. 4, we present qualitative comparisons between our method and two different baseline approaches, namely WDNNet [11] and ESDNet-L [7]. First, we observe that the stronger the baseline method employed, the better the moiré effect

removal. This is evident in both Case A and Case B, where employing ESDNet-L as the baseline method yields superior results. Furthermore, ShapeMoiré demonstrates advantages in moiré elimination and image detail restoration regardless of the baseline method’s strength. For instance, in Case A, the sailboat in the top row (b) and its surrounding sky appear to be more faithfully reproduced compared to those in (a). Similarly, in the bottom row of (b) where ESDNet-L is used as the baseline method, the color distribution of the lake surface appears more uniform compared to (a). In Case B, compared to the image in (a), the top row of (b) produced using ShapeMoiré not only eliminates the moiré pattern in the highlighted part of the image but also preserves the texture of the road. Similarly, in the bottom row, where ESDNet-L is the baseline method, the artifacts caused by the incomplete removal of moiré patterns in (b) are smaller compared to (a). All these observations underscore the superiority of our method.

To further validate the practicality of our proposed method, we captured real-world images using smartphones and applied both the baseline and ShapeMoiré methods to these cases, as depicted in Fig. 5. It is important to note that the patterns of moiré are not fixed; for the same original image, different devices may capture different moiré patterns, as illustrated



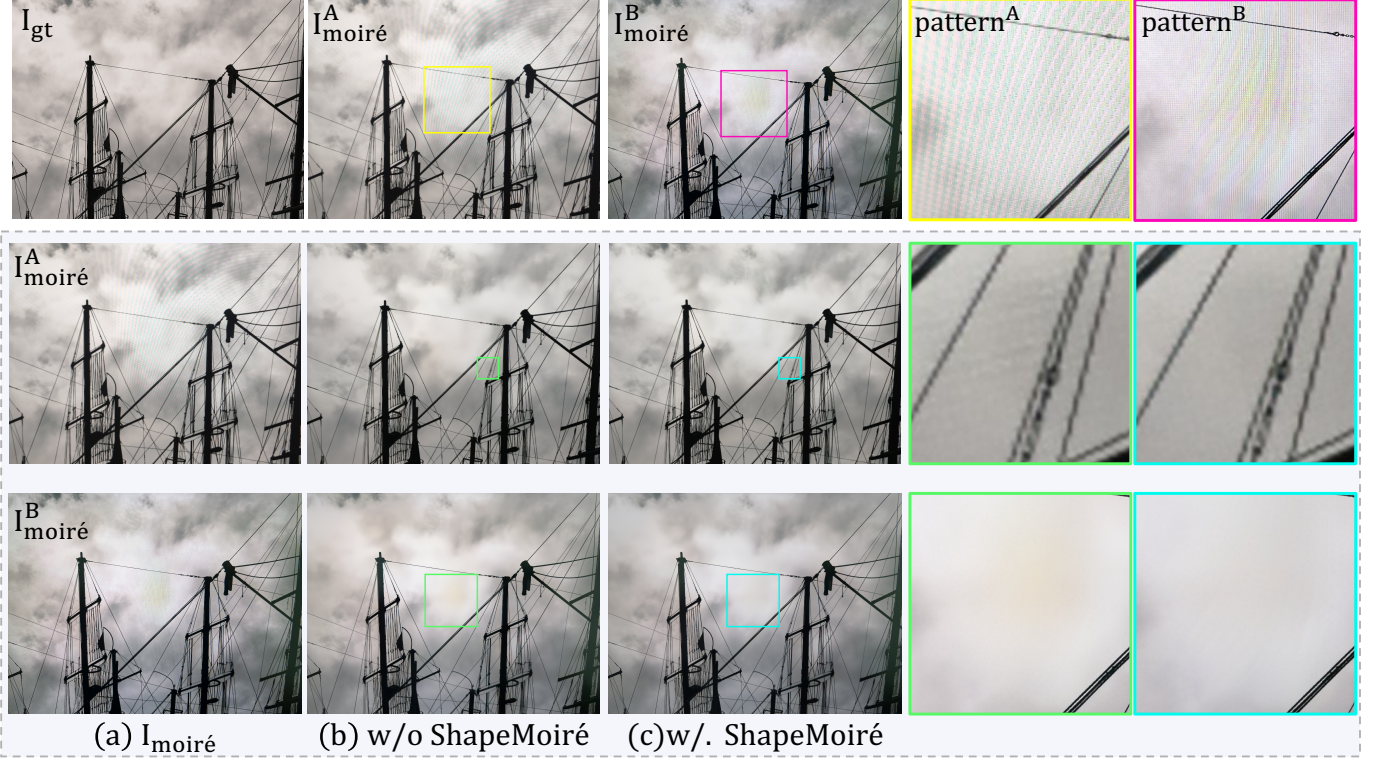


Fig. 5. Qualitative results of image demoiré for real-world cases. The selected samples are drawn from the UHDM dataset.  $I_{moiré}^A$  displays inputs from the dataset’s test samples, while  $I_{moiré}^B$  presenting real photos exhibiting moiré patterns captured using a smartphone. Larger boxes represent amplified views of the corresponding colored small boxes at the borders, offering a clearer perspective when enlarged.

by the two images with moiré, where  $I_{moiré}^A$  is the original input image in the UHDM dataset [7] and  $I_{moiré}^B$  is from our captured smartphone input image. It can be observed that  $I_{moiré}^A$  exhibits more widespread moiré artifacts across the entire region (*pattern*<sup>A</sup>), while in  $I_{moiré}^B$ , the artifacts are concentrated in the sky area at the center of the image (*pattern*<sup>B</sup>). From the results in Fig. 5, several observations can be made: 1) Our ShapeMoiré consistently outperforms the baseline method, regardless of the two morphologies of moiré,  $I_{moiré}^A$  and  $I_{moiré}^B$ ; our method exhibits superior moiré removal effects. 2) Our method demonstrates robustness against different moiré patterns, even helping alleviate color distortions. As shown in example  $I_{moiré}^B$  of Fig. 5, due to severe moiré in the blank sky area at the center, noticeable color deviations occur. ShapeMoiré not only excels in removing Moiré patterns but also effectively restores the true colors of the sky.

## V. CONCLUSION

In this paper, we extend our previously accepted ShapeConv to the image demoiré domain. Unlike existing methods, our proposed ShapeMoiré addresses the channel inconsistency problem of moiré patterns using *shape* features. The key extension in the method is the introduction of the Shape-Architecture, which models the *shape* information from the image-level and acts as a complement to the patch-level ShapeConv. The experimental results demonstrate its superiority over existing state-of-the-arts on four public popular datasets. Furthermore, we verify that our method can be

painlessly integrated into four strong baselines to improve their performance, while introducing negligible computational cost during inference. Additionally, our ShapeMoiré yields significant promise in real-world cases with irregular moiré patterns, making it potentially suitable for edge device application and deployment.

## REFERENCES

- [1] Y. Zhang, J. Liu, W. Yang, and Z. Guo, “Image super-resolution based on structure-modulated sparse representation,” *IEEE Transactions on Image Processing*, vol. 24, no. 9, pp. 2797–2810, 2015.
- [2] P. Wei, Z. Xie, G. Li, and L. Lin, “Taylor neural network for real-world image super-resolution,” *IEEE Transactions on Image Processing*, vol. 32, pp. 1942–1951, 2023.
- [3] C. Dong, Y. Deng, C. C. Loy, and X. Tang, “Compression artifacts reduction by a deep convolutional network,” in *Proceedings of the IEEE international conference on computer vision*, 2015, pp. 576–584.
- [4] J. Yang, F. Liu, H. Yue, X. Fu, C. Hou, and F. Wu, “Textured image demoiré via signal decomposition and guided filtering,” *IEEE Transactions on Image Processing*, vol. 26, no. 7, pp. 3528–3541, 2017.
- [5] B. He, C. Wang, B. Shi, and L.-Y. Duan, “Mop moiré patterns using mopnet,” in *Proceedings of the IEEE/CVF International Conference on Computer Vision*, 2019, pp. 2424–2432.
- [6] —, “Fhde 2 net: Full high definition demoiréing network,” in *Computer Vision—ECCV 2020: 16th European Conference, Glasgow, UK, August 23–28, 2020, Proceedings, Part XXII 16*. Springer, 2020, pp. 713–729.
- [7] X. Yu, P. Dai, W. Li, L. Ma, J. Shen, J. Li, and X. Qi, “Towards efficient and scale-robust ultra-high-definition image demoiréing,” in *European Conference on Computer Vision*. Springer, 2022, pp. 646–662.
- [8] H. Yue, Y. Cheng, Y. Mao, C. Cao, and J. Yang, “Recaptured screen image demoiréing in raw domain,” *IEEE Transactions on Multimedia*, 2022.

- [9] S. Yuan, R. Timofte, G. Slabaugh, A. Leonardis, B. Zheng, X. Ye, X. Tian, Y. Chen, X. Cheng, Z. Fu et al., "Aim 2019 challenge on image demoiréing: Methods and results," in *2019 IEEE/CVF International Conference on Computer Vision Workshop (ICCVW)*. IEEE, 2019, pp. 3534–3545.
- [10] Y. Sun, Y. Yu, and W. Wang, "Moiré photo restoration using multi-resolution convolutional neural networks," *IEEE Transactions on Image Processing*, vol. 27, no. 8, pp. 4160–4172, 2018.
- [11] L. Liu, J. Liu, S. Yuan, G. Slabaugh, A. Leonardis, W. Zhou, and Q. Tian, "Wavelet-based dual-branch network for image demoiréing," in *Computer Vision–ECCV 2020: 16th European Conference, Glasgow, UK, August 23–28, 2020, Proceedings, Part XIII 16*. Springer, 2020, pp. 86–102.
- [12] B. Zheng, S. Yuan, G. Slabaugh, and A. Leonardis, "Image demoiréing with learnable bandpass filters," in *Proceedings of the IEEE/CVF conference on computer vision and pattern recognition*, 2020, pp. 3636–3645.
- [13] J. Cao, H. Leng, D. Lischinski, D. Cohen-Or, C. Tu, and Y. Li, "Shapeconv: Shape-aware convolutional layer for indoor rgb-d semantic segmentation," in *Proceedings of the IEEE/CVF international conference on computer vision*, 2021, pp. 7088–7097.
- [14] <https://digitalanarchy.com/Flicker/main.html>.
- [15] B. Liu, X. Shu, and X. Wu, "Demoiréing of camera-captured screen images using deep convolutional neural network," *arXiv preprint arXiv:1804.03809*, 2018.
- [16] X. Cheng, Z. Fu, and J. Yang, "Multi-scale dynamic feature encoding network for image demoiréing," in *2019 IEEE/CVF International Conference on Computer Vision Workshop (ICCVW)*. IEEE, 2019, pp. 3486–3493.
- [17] J. Liang, J. Cao, G. Sun, K. Zhang, L. Van Gool, and R. Timofte, "Swinir: Image restoration using swin transformer," in *Proceedings of the IEEE/CVF international conference on computer vision*, 2021, pp. 1833–1844.
- [18] S. W. Zamir, A. Arora, S. Khan, M. Hayat, F. S. Khan, M.-H. Yang, and L. Shao, "Multi-stage progressive image restoration," in *Proceedings of the IEEE/CVF conference on computer vision and pattern recognition*, 2021, pp. 14 821–14 831.
- [19] S. W. Zamir, A. Arora, S. Khan, M. Hayat, F. S. Khan, and M.-H. Yang, "Restormer: Efficient transformer for high-resolution image restoration," in *Proceedings of the IEEE/CVF conference on computer vision and pattern recognition*, 2022, pp. 5728–5739.
- [20] O. Ronneberger, P. Fischer, and T. Brox, "U-net: Convolutional networks for biomedical image segmentation," in *Medical image computing and computer-assisted intervention–MICCAI 2015: 18th international conference, Munich, Germany, October 5-9, 2015, proceedings, part III 18*. Springer, 2015, pp. 234–241.
- [21] H. Zhang, Y. Dai, H. Li, and P. Koniusz, "Deep stacked hierarchical multi-patch network for image deblurring," in *Proceedings of the IEEE/CVF conference on computer vision and pattern recognition*, 2019, pp. 5978–5986.
- [22] C. Dong, C. C. Loy, K. He, and X. Tang, "Learning a deep convolutional network for image super-resolution," in *Computer Vision–ECCV 2014: 13th European Conference, Zurich, Switzerland, September 6-12, 2014, Proceedings, Part IV 13*. Springer, 2014, pp. 184–199.
- [23] K. Zhang, W. Zuo, Y. Chen, D. Meng, and L. Zhang, "Beyond a gaussian denoiser: Residual learning of deep cnn for image denoising," *IEEE transactions on image processing*, vol. 26, no. 7, pp. 3142–3155, 2017.
- [24] W.-S. Lai, J.-B. Huang, N. Ahuja, and M.-H. Yang, "Deep laplacian pyramid networks for fast and accurate super-resolution," in *Proceedings of the IEEE conference on computer vision and pattern recognition*, 2017, pp. 624–632.
- [25] K. Zhang, W. Zuo, and L. Zhang, "Learning a single convolutional super-resolution network for multiple degradations," in *Proceedings of the IEEE conference on computer vision and pattern recognition*, 2018, pp. 3262–3271.
- [26] L. Wang, Y. Wang, Z. Liang, Z. Lin, J. Yang, W. An, and Y. Guo, "Learning parallax attention for stereo image super-resolution," in *Proceedings of the IEEE/CVF conference on computer vision and pattern recognition*, 2019, pp. 12 250–12 259.
- [27] K. He, X. Zhang, S. Ren, and J. Sun, "Deep residual learning for image recognition," in *Proceedings of the IEEE conference on computer vision and pattern recognition*, 2016, pp. 770–778.
- [28] G. Huang, Z. Liu, L. Van Der Maaten, and K. Q. Weinberger, "Densely connected convolutional networks," in *Proceedings of the IEEE conference on computer vision and pattern recognition*, 2017, pp. 4700–4708.
- [29] Z. Xiong, S. Chen, Y. Wang, L. Mou, and X. X. Zhu, "Gamus: A geometry-aware multi-modal semantic segmentation benchmark for remote sensing data," *arXiv preprint arXiv:2305.14914*, 2023.
- [30] J. Zhong, M. Li, H. Zhang, and J. Qin, "Combining photogrammetric computer vision and semantic segmentation for fine-grained understanding of coral reef growth under climate change," in *Proceedings of the IEEE/CVF Winter Conference on Applications of Computer Vision*, 2023, pp. 186–195.
- [31] Q. Zhou, J. Cao, H. Leng, Y. Yin, Y. Kun, and R. Zimmermann, "Sogdet: Semantic-occupancy guided multi-view 3d object detection," in *Proceedings of the AAAI Conference on Artificial Intelligence*, vol. 38, no. 7, 2024, pp. 7668–7676.
- [32] Y. Zhang, M. Lin, X. Li, H. Liu, G. Wang, F. Chao, S. Ren, Y. Wen, X. Chen, and R. Ji, "Real-time image demoiréing on mobile devices," *arXiv preprint arXiv:2302.02184*, 2023.
- [33] S. Xu, B. Song, X. Chen, and J. Zhou, "Image demoiréing in raw and srgb domains," *arXiv preprint arXiv:2312.09063*, 2023.
- [34] H. Wang, Q. Tian, L. Li, and X. Guo, "Image demoiréing with a dual-domain distilling network," in *ICME*. IEEE, 2021, pp. 1–6.
- [35] J. Deng, W. Dong, R. Socher, L.-J. Li, K. Li, and L. Fei-Fei, "Imagenet: A large-scale hierarchical image database," in *2009 IEEE conference on computer vision and pattern recognition*. Ieee, 2009, pp. 248–255.
- [36] Z. Wang, A. C. Bovik, H. R. Sheikh, and E. P. Simoncelli, "Image quality assessment: from error visibility to structural similarity," *IEEE transactions on image processing*, vol. 13, no. 4, pp. 600–612, 2004.
- [37] R. Zhang, P. Isola, A. A. Efros, E. Shechtman, and O. Wang, "The unreasonable effectiveness of deep features as a perceptual metric," in *Proceedings of the IEEE conference on computer vision and pattern recognition*, 2018, pp. 586–595.

## APPENDIX

*Proof.*

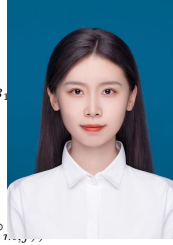
$$\begin{aligned}
\mathbb{F}_{c_{out}} &= \sum_k^{K_h \times K_w \times C_{in}} (\mathbb{K}_{k,c_{out}} \times \mathbf{P}_{BS_k}) \\
&= \sum_i^{K_h \times K_w} \sum_j^{C_{in}} (\mathbb{K}_{i,j,c_{out}} \times \mathbf{P}_{BS_{i,j}}) \\
&= \sum_i^{K_h \times K_w} \sum_j^{C_{in}} (\mathbb{K}_{i,j,c_{out}} \times (\mathbf{P}_{B_{1,j}} + \mathbf{P}_{S_{i,j}})) \\
&= \sum_i^{K_h \times K_w} \sum_j^{C_{in}} (\mathbb{K}_{i,j,c_{out}} \times (\mathbb{W}_B \times \mathbb{P}_{B_{1,j}} \\
&\quad + \sum_m^{K_h \times K_w} (\mathbb{W}_{S_{m,i,j}} \times \mathbb{P}_{S_{m,j}}))) \\
&= \sum_i^{K_h \times K_w} \sum_j^{C_{in}} (\mathbb{W}_B \times \mathbb{K}_{i,j,c_{out}} \times \mathbb{P}_{B_{1,j}} \\
&\quad + \sum_m^{K_h \times K_w} (\mathbb{W}_{S_{m,i,j}} \times \mathbb{K}_{i,j,c_{out}} \times \mathbb{P}_{S_{m,j}})) \\
&= \sum_i^{K_h \times K_w} \sum_j^{C_{in}} (\mathbb{W}_B \times \mathbb{K}_{B_{1,j},c_{out}} \times \mathbb{P}_{i,j} \\
&\quad + \sum_m^{K_h \times K_w} (\mathbb{W}_{S_{m,i,j}} \times \mathbb{K}_{i,j,c_{out}} \times (\mathbb{P}_{m,j} - \mathbb{P}_{B_{1,j}}))) \\
&= \sum_i^{K_h \times K_w} \sum_j^{C_{in}} (\mathbf{K}_{B_{1,j},c_{out}} \times \mathbb{P}_{i,j}) \\
&\quad + \sum_i^{K_h \times K_w} \sum_j^{C_{in}} \sum_m^{K_h \times K_w} (\mathbb{W}_{S_{m,i,j}} \times \mathbb{K}_{i,j,c_{out}} \times \mathbb{P}_{m,j} - \mathbb{W}_{S_{m,i,j}} \times \mathbb{K}_{i,j,c_{out}} \times \mathbb{P}_{B_{1,j}}) \\
&= \sum_i^{K_h \times K_w} \sum_j^{C_{in}} (\mathbf{K}_{B_{1,j},c_{out}} \times \mathbb{P}_{i,j}) \\
&\quad + \sum_i^{K_h \times K_w} \sum_j^{C_{in}} \sum_m^{K_h \times K_w} (\mathbb{W}_{S_{m,i,j}} \times \mathbb{K}_{i,j,c_{out}} \times \mathbb{P}_{m,j} - \mathbb{W}_{S_{m,i,j}} \times \mathbb{K}_{B_{1,j},c_{out}} \times \mathbb{P}_{i,j}) \\
&= \sum_i^{K_h \times K_w} \sum_j^{C_{in}} (\mathbf{K}_{B_{1,j},c_{out}} \times \mathbb{P}_{i,j}) \\
&\quad + \sum_i^{K_h \times K_w} \sum_j^{C_{in}} \sum_m^{K_h \times K_w} (\mathbb{W}_{S_{m,i,j}} \times (\mathbb{K}_{i,j,c_{out}} - \mathbb{K}_{B_{1,j},c_{out}}) \times \mathbb{P}_{m,j}) \\
&= \sum_i^{K_h \times K_w} \sum_j^{C_{in}} (\mathbf{K}_{B_{1,j},c_{out}} \times \mathbb{P}_{i,j}) \\
&\quad + \sum_i^{K_h \times K_w} \sum_j^{C_{in}} \sum_m^{K_h \times K_w} (\mathbb{W}_{S_{m,i,j}} \times \mathbb{K}_{S_{i,j},c_{out}} \times \mathbb{P}_{m,j}) \\
&= \sum_i^{K_h \times K_w} \sum_j^{C_{in}} (\mathbf{K}_{B_{1,j},c_{out}} \times \mathbb{P}_{i,j}) \\
&\quad + \sum_m^{K_h \times K_w} \sum_j^{C_{in}} (\mathbf{K}_{S_{m,j},c_{out}} \times \mathbb{P}_{m,j}) \\
&= \sum_i^{K_h \times K_w} \sum_j^{C_{in}} (\mathbf{K}_{B_{1,j},c_{out}} \times \mathbb{P}_{i,j} + \mathbf{K}_{S_{i,j},c_{out}} \times \mathbb{P}_{i,j}) \\
&= \sum_i^{K_h \times K_w} \sum_j^{C_{in}} ((\mathbf{K}_{B_{1,j},c_{out}} + \mathbf{K}_{S_{i,j},c_{out}}) \times \mathbb{P}_{i,j}) \\
&= \sum_i^{K_h \times K_w} \sum_j^{C_{in}} (\mathbf{K}_{BS_{i,j},c_{out}} \times \mathbb{P}_{i,j}) \\
&= \sum_k^{K_h \times K_w \times C_{in}} (\mathbf{K}_{BS_k,c_{out}} \times \mathbb{P}_k)
\end{aligned}$$



**Jinming Cao** received her Ph.D. with the School of Computer Science and Technology from Shandong University in 2022. She is currently working as a Research Fellow with the National University of Singapore. Her research interests include computer vision and 3D vision.



**Sicheng Shen** is currently an undergraduate student at the Faculty of Science, National University of Singapore. His research interest includes computer vision.



**Qiu Zhou** received the Master degree with the School of Computer Science and Technology from Shandong University in 2022. She is currently a Ph.D. student with the Beijing University of Posts and Telecommunications. Her research interests include computer vision and 3D vision.



**Yifang Yin** received the BE degree from the Department of Computer Science and Technology, Northeastern University, Shenyang, China, in 2011 and the PhD degree from the National University of Singapore, Singapore, in 2016. She is currently a senior scientist with Institute for Infocomm Research (I<sup>2</sup>R) in the Agency for Science, Technology and Research, Singapore (A\*STAR). She also holds an adjunct faculty position with IIIT-Delhi. Before joining A\*STAR, she worked as a senior research fellow with the Grab-NUS AI Lab with the National University of Singapore. She also worked as a Research Intern with the Incubation Center, Research and Technology Group, Fuji Xerox Co., Ltd., Japan, from October, 2014 to March, 2015. Her research interests include machine learning, spatiotemporal data mining, and multimodal analysis in multimedia.



**Yangyan Li** received his Ph.D. from University of Chinese Academy of Sciences in 2013. He is currently working in Alibaba group. Before that, he was a professor in Shandong University, and Postdoc in Stanford University and Tel Aviv University. His research interests include computer graphics and computer vision, with an emphasis on 3D learning and vision.





**Roger Zimmermann** received the M.S. and Ph.D. degrees from the Viterbi School of Engineering at the University of Southern California. He is a Full Professor at the School of Computing at the National University of Singapore (NUS). He is a Co-PI with the Grab-NUS AI Lab. His research interests are streaming media architectures and protocols for video (DASH) and immersive media (e.g., point cloud data), applications of machine/deep learning, spatiotemporal data management, analytics and applications, and location-based services.